Computers & Geosciences 131 (2019) 158–169

Contents lists available at ScienceDirect

Computers and Geosciences

journal homepage: www.elsevier.com/locate/cageo

Research paper

Efficient parallel random field generator for large 3-D geophysical problems

Ludovic Räss [a,b,c,*], Dmitriy Kolyukhin [d], Alexander Minakov [e]

[a] Stanford University, Geophysics Department, 397 Panama Mall, Stanford CA 94305, USA
[b] Institute of Earth Sciences, University of Lausanne, Lausanne, Switzerland
[c] Swiss Geocomputing Centre, University of Lausanne, Lausanne, Switzerland
[d] Trofimuk Institute of Petroleum Geology and Geophysics SB RAS, pr. Koptyuga, 3, 630090, Novosibirsk, Russia
[e] Centre for Earth Evolution and Dynamics (CEED), University of Oslo, Norway

ARTICLE INFO

Keywords:
Geophysics
Geostatistics
Seismology
Computational methods
Parallel and high-performance computing

ABSTRACT

We present an efficient implementation of the method for sampling spatial realisations of a 3-D random fields with given power spectrum. The method allows for a multi-scale resolution and approaches well for parallel implementations, overcoming the physical limitation of computer memory when dealing with large 3-D problems. We implement the random field generator to execute on graphical processing units (GPU) using the CUDA C programming language. We compare the memory footprint and the wall-time of our implementation to FFT-based solutions. We illustrate the efficiency of the proposed numerical method using examples of an acoustic scattering problem which can be encountered both in controlled-source and earthquake seismology. In particular, we apply our method to study the scattering of seismic waves in 3-D anisotropic random media with a particular focus on P-wave coda observations and seismic monitoring of hydrocarbon reservoirs.

1. Introduction

Incomplete data and complex nature of geophysical phenomena leads to the need for statistical modelling. The results of this approach can also be used, for example, for sensitivity analysis or uncertainty quantification. Stochastic simulations of random fields with multi-scale resolution have found application in studies of turbulent flows (Minakov et al., 2017; Kurbanmuradov et al., 1997; Kraichnan, 1970), flow in porous media (Kolyukhin and Sabelfeld, 2005), seismic volcanology (Sato et al., 2012; De Siena et al., 2013), large-scale density structure of the universe (Sabelfeld and Loshchina, 2010) and other geophysical and astrophysical problems. Some other geoscience applications and simulation techniques are described in the monograph by Christakos (2012).

One of the important applications of the random field simulation in computational geophysics is linked to numerical mechanical modelling. Numerical analysis of large mechanical problems with severe nonlinearities such as flow localisation in two-phase deformable media (Räss et al., 2018) or simulation of fracture networks and dike swarms (Minakov et al., 2018) rely on a model initialisation procedure including computation of random field of small parameter perturbation (e.g. porosity or rock cohesion). The important requirement is that both large and small spatial scales must be accurately resolved by the numerical grid to obtain a physically meaningful solution.

Some geophysical inverse problems directly target on statistical properties of the medium (e.g. ocean temperature fluctuation spectra, lithosphere gravity-topography spectral ratios, scattering strength and attenuation spectra from seismic coda waves). For this class of problems proving the parameter sensitivity and model resolution requires a random field simulator (RFS) reproducing observed statistical behaviour of the physical process such as correlation function or power spectrum within a broad range of scales. The accurate statistics is also required for inverse geophysical problems formulated as a Bayesian inference problem with physically-based prior distribution (Hansen et al., 2008).

Cholesky decomposition of the covariance matrix is perhaps the most well-known method to generate the realisations of Gaussian random fields. This method is based on a clear idea, simple in use, and allows in addition to perform conditional simulations to adapt the measurement data. However, as the number of grid points increases, this method becomes very computationally time consuming. The turning-band method (Mantoglou and Wilson, 1982) and spectral method (Robin et al., 1993) are among other frequently utilised approaches for modelling random fields. An efficient method for sampling random realisations, based on fast Fourier transform (FFT) moving-average method was developed in Le Ravalec et al. (2000). The comparative analysis of Fourier-wavelet simulation method against spectral method with different randomisations of wavenumber space is performed in Kramer et al. (2007). The Karhunen–Loève expansion based

* Corresponding author at: Stanford University, Geophysics Department, 397 Panama Mall, Stanford CA 94305, USA.
E-mail address: ludovic.rass@gmail.com (L. Räss).

https://doi.org/10.1016/j.cageo.2019.06.007
Received 18 October 2018; Received in revised form 29 May 2019; Accepted 11 June 2019
Available online 2 July 2019

on finding the eigenvalues and eigenvectors of the covariance function can be used to simulate non-homogeneous random fields (Phoon et al., 2002). In Phoon et al. (2005) this technique was extended for simulation of strongly non-Gaussian random fields. Another method that allows one to model more complex non-homogeneous and non-Gaussian fields is to use Polynomial Chaos extension (Xiu and Karniadakis, 2002).

A number of methods for indicator random fields simulation that can have discrete values have been developed (Dowd et al., 2007). For simple geological models, the simulation of the indicator random fields with given mean values and the covariance function can be achieved using a truncated Gaussian simulation (TGS). This method is based on the use of an auxiliary Gaussian random field constructed by the methods described above. For more complex geological models, a more general truncated PluriGaussian simulation (TPGS) was developed (Dowd et al., 2003). TGS and TPGS are based on the reproduction of two-point statistics (covariance or variogram functions). These methods have a number of limitations when modelling structures with a complex curvilinear geometry (for example, media with channels). In recent years, the usages of statistical modelling methods relying on multipoint statistics increased (Strebelle, 2002; Tang et al., 2013). One more approach to statistical modelling is based on the use of optimisation methods such as the simulated annealing, which requires to consider some objective functions (Deutsch and Cockerham, 1994). For example, Tran et al. (2007) use this approach to simulate the spatial distribution of a fracture network. A new Gibbs sampler for simulation of Gaussian Markov random fields on large lattice was developed recently in Marcotte and Allard (2018).

Fast spectral methods based on the FFT are traditionally used in seismology (Holliger et al., 1993; Sato et al., 2012; Meschede and Romanowicz, 2015). The disadvantage of this approach is the need to generate the values of the realisation of a random field in all nodes of the computational domain. Moreover, a computation on an irregular grid is difficult using this method.

We present here a parallel implementation of the method based on spectral representation described in Sabelfeld (1991). Advantages of this method are the possibility of random field simulation on an arbitrary grid and the simplicity of parallel implementation of the algorithm. The method is flexible and is also applicable for arbitrary anisotropic spectrums. Moreover, at present this simulation technique is well studied. For example, ergodicity properties were studied by Kramer et al. (2007).

Serial algorithms are bottleneck for three-dimensional (3-D) computations. Routines that rely on local operation only can perform very efficiently on actual parallel hardware, such as graphical processing units (GPUs). Calculating every grid point of the computational domain on a distinct hardware thread permits thus to achieve a fast time to solution using performance-oriented software. In particular, the method presented in this paper is shown to be more flexible for large simulations than FFT-based methods and follows similar path as de Carvalho Paludo et al. (2015).

We provide a recipe to efficiently compute a 3-D random fields with a known power spectrum or correlation function making a particular focus on geophysical applications. The presented GRFS (exponential and Gaussian covariance) algorithm and computer codes (Matlab & GPU-based CUDA C) are provided as supplementary material and available for download from Bitbucket at https://bitbucket.org/lraess/GRFS and from the Swiss Geocomputing Centre website http://wp.unil.ch/geocomputing/software/grfs/. The GPU cuFFT-based benchmarking algorithm as well as the GPU-based 3-D acoustic wave propagation software can be obtained upon request from the authors.

2. Random field generator based on spectral representation

In this work we assume that the scalar random field $f(\mathbf{x})$ is statistically homogeneous with a mean value $m_f(\mathbf{x})$. The probability density function of a scalar Gaussian random field $f(\mathbf{x})$ in the points $\mathbf{x} = \{\mathbf{x}_1, \dots, \mathbf{x}_n\}$

$$p(f(\mathbf{x}_1), \dots, f(\mathbf{x}_n)) = \frac{1}{(2\pi \ \det C_{ff})^{1/2}} \times \exp\left\{-\frac{1}{2}(f(\mathbf{x}) - \mathbf{m})^T C_{ff}^{-1}(f(\mathbf{x}) - \mathbf{m})\right\} \quad (1)$$

is fully defined by its mean values $\mathbf{m} = \{m_1, \dots, m_n\}$ and the covariance function $C_{ff}(\mathbf{x}_i, \mathbf{x}_j) = \langle (f(\mathbf{x}_i) - m_i)(f(\mathbf{x}_j) - m_j)\rangle$. We use bold font for vectors, $\langle\cdot\rangle$ – is a mathematical expectation.

The covariance function and the spectrum of homogeneous random fields are related through the equation:

$$S_{ff}(\mathbf{k}) = \frac{1}{8\pi^3}\int_{R^3} e^{-i(\mathbf{r},\mathbf{k})} C_{ff}(\mathbf{r}) d\mathbf{r} \ . \quad (2)$$

The simulation formula based on the spectral randomisation method has the form:

$$f(\mathbf{x}) = m_f(\mathbf{x}) + \frac{\sigma_f}{\sqrt{N_h}} \sum_{i=1}^{N_h} \left[\xi_i \cos(\mathbf{k}_i, \mathbf{x}) + \eta_i \sin(\mathbf{k}_i, \mathbf{x})\right] \quad (3)$$

and can be used for random field generation (Sabelfeld, 1991). Here ξ_i and η_i – are mutually independent and independent on $\mathbf{k}_i$ random numbers with zero mean and variance equal to unity, $(\mathbf{k}_i, \mathbf{x})$ – is the scalar product of the vectors $\mathbf{k}_i$ and $\mathbf{x}$. Following Sabelfeld (1991), the wave vector $\mathbf{k}$ is sampled according to the probability density

$$p(\mathbf{k}) \propto \frac{S_{ff}(\mathbf{k})}{\int_{R^3} S_{ff}(\mathbf{k}) d\mathbf{k}} \ . \quad (4)$$

The central limit theorem provides that $f(\mathbf{x})$ will converge to Gaussian distributions as the number of harmonics $N_h \to \infty$ (Sabelfeld, 1991).

The presented approach is general and can be applied for any homogeneous covariance C_{ff} and corresponding S_{ff}. The key insight in this technique is the sampling of the wave vector $\mathbf{k}$ according to the probability density (4). The general approaches for the sampling are described for example in Rubinstein (1981) and Sabelfeld (1991).

In this work, we mainly consider an anisotropic exponential covariance which is most often used in geosciences applications

$$C_{ff}(\mathbf{r}) = \sigma_f^2 \exp\left\{-\left(\frac{r_1^2}{I_1^2} + \frac{r_2^2}{I_2^2} + \frac{r_3^2}{I_3^2}\right)^{1/2}\right\} , \quad (5)$$

where $\mathbf{r} = (r_1, r_2, r_3)$ – is a separation vector, σ_f – is a standard deviation and I_j, $j = 1, 2, 3$ — are correlation lengths in jth direction. Following Eyink and Goldenfeld (1994) the correlation length is defined as:

$$I_j = \frac{1}{C_{ff}(0)}\int_0^\infty C_{ff}(r_j) dr_j \ . \quad (6)$$

Note, that other definitions of correlation length also appear in the scientific literature (Simonovski and Cizelj, 2005; Tyaginov et al., 2009); for example, the length r for which

$$C_{ff}(\mathbf{r}) = C_{ff}(0)/e \ . \quad (7)$$

The covariance function (5) corresponds to the spectrum:

$$S_{ff}(\mathbf{k}) = \frac{\sigma_f^2 I_1 I_2 I_3}{\pi^2(1 + I_1^2 k_1^2 + I_2^2 k_2^2 + I_3^2 k_3^2)^2} \ , \quad (8)$$

where $\mathbf{k} = (k_1, k_2, k_3)$ is a wave vector.

To generate the realisations of the vector $\mathbf{k}$, the following formulas are used:

$$\begin{cases} k_1 = k\cos(\theta)/I_1 \ , \\ k_2 = k\cos(\phi)\sin(\theta)/I_2 \ , \\ k_3 = k\sin(\phi)\sin(\theta)/I_3 \ . \end{cases} \quad (9)$$

The scalar value k is distributed with the probability distribution

$$p(k) = \frac{4k^2}{\pi(1+k^2)^2} \ . \tag{10}$$

Its realisations can be generated using the rejection method, described in Rubinstein (1981). The value of the angle ϕ is sampled uniformly in the interval $[0, 2\pi]$, the value θ is distributed with the probability density

$$p(\theta) = \frac{1}{2}\sin(\theta), \ \theta \in [0, \pi] \ . \tag{11}$$

The corresponding simulation formula has the form

$$\theta = \arccos(1 - 2\lambda) \ , \tag{12}$$

where λ – is a random value uniformly distributed in $[0, 1]$. The implementation of the anisotropic exponential covariance Gaussian random field is presented in Algorithm 1 (Section 4).

For comparison we also consider the isotropic Gaussian correlation function

$$C_{ff}(\mathbf{r}) = \sigma_f^2 \exp\left\{-\frac{r_1^2}{l_f^2}\right\}, \tag{13}$$

with correlation length $I_f = l_f \frac{\sqrt{\pi}}{2}$. The corresponding spectrum (Monin and Yaglom, 1971) has the form:

$$S_{ff}(\mathbf{k}) = \frac{\sigma^2 l_f^3}{8\pi^{3/2}} \exp\left(-\frac{k^2 l_f^2}{4}\right) \ . \tag{14}$$

In this case, the scalar wave number is proportional to:

$$p(k') = k'^2 \exp\left(-\frac{k'^2}{2}\right) \ , \ k' = k\frac{l_f}{\sqrt{2}} \ . \tag{15}$$

These numbers can be generated by using the rejection method (Rubinstein, 1981). The implementation of the isotropic Gaussian covariance alternative is presented in Algorithm 2 (Section 4).

3. Random field generator based on Fast Fourier transform

Further, the random field modelling method presented in the previous section is compared with the most effective to our knowledge and frequently used method for modelling of homogeneous random fields based on the Fast Fourier transform (Katz and Weatherley, 2012; Le Ravalec et al., 2000; Sava and Poliannikov, 2008).

Direct $F = FFT(f)$ and inverse $f = FFT^{-1}(F)$ Fast Fourier transformations are:

$$F(j) = \sum_{k=0}^{N-1} f(k) exp(2\pi ikj/N) \ , \tag{16}$$

$$f(k) = \sum_{j=0}^{N-1} F(j) exp(-2\pi ikj/N) \ , \tag{17}$$

where N is the number of sampled points.

The simulation formula takes the following form:

$$f(\mathbf{x}) = m_f(\mathbf{x}) + FFT^{-1}\left[\sqrt{FFT(C_{ff}(\mathbf{x}))}FFT(Z(\mathbf{x}))\right] \ , \tag{18}$$

where $Z(\mathbf{x})$ are independent Gaussian random numbers with zero mean and unit variance.

It is important to emphasise that due to the periodicity of the FFT within the simulation we can only use the $f(\mathbf{x})$ values generated for the inner subdomain. In consequence, the realisations should be oversized at the beginning and at the end of the domain; the near-border cells must be removed (Le Ravalec et al., 2000). We recommend using an indent distance equal to at least two correlation lengths.

4. Numerical implementation

The motivation driving the development of the random field generator based on spectral representation is to propose an algorithm that runs efficiently and scales on parallel hardware, such as GPUs. These many-core accelerators are capable to efficiently perform a large number of identical tasks in parallel. This is of particular interest when performing simulations on large computational domains, inherent to 3-D calculations. However, efficient parallel algorithms strongly rely on local operations. For optimal performance, each parallel process (also called thread) may perform the workflow tasks independently, implying no communication with neighbouring threads, neither waiting on other processes to accomplish their tasks first. The proposed method to generate Gaussian random fields based on the spectral representation fulfils both aforementioned requirements; only the spatial coordinates of each grid point within the computational domain are mandatory and can be determined in a straight forward way. The inherent parallelism of the approach is thus very well suited for GPU computing. Each thread is responsible to compute one grid point of the domain based on its coordinate, without need of any communication neither global reduction operations. Irregular grid spacing can easily be obtained by choosing indices of spatial coordinates to be non-uniform.

Algorithm 1 Gaussian random field simulator – Exponential covariance

```
1: C = sigf/sqrt(N_h)
2: for (ih = 0; ih < N_h; ih++) do
3:     fi = 2 π rand
4:     flag = 1
5:     while (flag = 1) do
6:         k = tan(π 0.5 rand)
7:         d = k^2/(1 + k^2)
8:         if (rand < d) then
9:             flag = 0
10:        end if
11:    end while
12:    theta = acos(1 − 2 rand)
13:    V_1 = k sin(fi) sin(theta)/I_1
14:    V_2 = k cos(fi) sin(theta)/I_2
15:    V_3 = k cos(theta)/I_3
16:    a = randn
17:    b = randn
18:    compute_kernel_1 <<< grid, block >>> ();
       cudaDeviceSynchronize()
19: end for
20: compute_kernel_2 <<< grid, block >>> (); cudaDeviceSynchronize()
```

The algorithm is composed of three main blocks; (1) the host code (executed by the host — the central processing unit or CPU) and common to the entire spatial domain (Algorithm 1 — exponential covariance or Algorithm 2 — Gaussian covariance) containing the outer loop over a given (large) number of harmonics N_h, precomputing the wave vector, and calling the two GPU functions (also called kernels) named compute_kernel; (2) the first GPU compute kernel (Algorithm 3) calculates the random field values in parallel (3) for every thread based on the wave vectors input; (3) the second compute kernel (Algorithm 4) multiplies the random field values by a constant and must be located outside the outer loop over the harmonics.

We implemented the algorithm using C and the CUDA extension in order to execute the application in parallel on Nvidia GPUs. CUDA provides as main feature a vectorised framework allowing to execute the serial loop over each spatial dimension in parallel by the mean of their *thread*, *block* and *grid* layout (Nvidia, 2018).

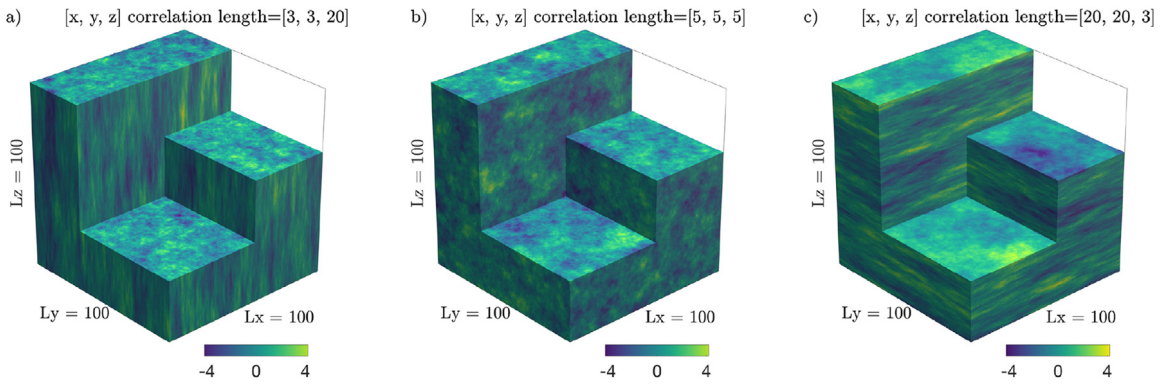

Fig. 1. Simulated random field for different correlation lengths in all three spatial dimensions within a cube of size [100, 100, 100] in x, y and z direction, respectively. (a) Vertical tube-like random media, with correlation length of [3, 3, 20] in x, y and z directions, respectively. (b) Isotropic random media, with correlation length of [5, 5, 5] in all three directions. (c) Horizontal planar-like random media, with correlation length of [20, 20, 3] in x, y and z directions, respectively.

Algorithm 2 Gaussian random field simulator – Gaussian covariance

```
C = sigf/sqrt(N_h)
lf = 2 I/sqrt(π)
for (ih = 0; ih < N_h; ih++) do
    fi = 2 π rand
    flag = 1
    while (flag = 1) do
        k = k_max rand
        d = k^2 exp(−0.5 k^2)
        if (2 rand exp(−1) < d) then
            flag = 0;
        end if
    end while
    k = k sqrt(2)/lf
    theta = acos(1 − 2 rand)
    V_1 = k sin(fi) sin(theta)
    V_2 = k cos(fi) sin(theta)
    V_3 = k cos(theta)
    a = randn
    b = randn
    compute_kernel_1 <<< grid, block >>> ();
    cudaDeviceSynchronize()
end for
compute_kernel_2 <<< grid, block >>> (); cudaDeviceSynchronize()
```

Algorithm 3 compute_kernel_1

```
tmp = dx((ix + 1) − 0.5)V_1 + dy((iy+1) − 0.5)V_2 + dz((iz + 1) − 0.5)V_3
Yf = Yf + a sin(tmp) + b cos(tmp)
```

Algorithm 4 compute_kernel_2

```
Yf = C Yf
```

We generate uniformly distributed in [0,1] random numbers ('rand') within the algorithm using the C built-in pseudo random number generator rand() and normalise the output (using RAND_MAX) to the range $[0, 1]$ within the RND() macro. To obtain standard normal random numbers ('randn') in the range $[-\infty, \infty]$, we rely on the Box–Muller algorithm (Box and Muller, 1958) within the RNDN() macro implementation:

$$\text{randn} = \sqrt{-2\ \log(\lambda_1)}\ \cos(2\pi\lambda_2) \tag{19}$$

where λ_1 and λ_2 are two independent random numbers uniformly distributed in [0,1] and obtained via the 'rand' routine.

Both single and double precision arithmetic is available to simulate the random field within the routines. Some basic sensitivity analysis suggests that single precision arithmetic delivers comparable results as double precision calculation for the here described purpose. This provides a non-negligible advantage since single precision arithmetic calculations require twice less memory to be transferred when compared to double precision. Single precision calculations are thus twice more efficient in terms of execution time compared to double precision ones for memory bounded algorithms.

5. Results

5.1. Anistropic random field realisations

The outcome of the random field simulator are 3-D domains that depict various correlation lengths in all three spatial dimensions (Fig. 1). The user defined input variables are the box size, the standard deviation of the Gaussian random field, the x, y and z correlation lengths and the number of harmonics (N_h).

5.2. Benchmarks

Within this study we mainly showcase the usage of the exponential covariance function to generate Gaussian random fields, However, the approach we propose here generalises to other covariance functions, such as the Gaussian isotropic covariance (Fig. 2). We perform three different benchmarks to validate both the presented approach for simulating Gaussian random fields using (a) an anisotropic exponential covariance function and (b) an isotropic Gaussian covariance function and thus highlight the potential of the method. Finally, we discuss the numerical implementation on GPUs and report performance results comparing our random field generator based on spectral representations to well-established FFT-based routines in terms of wall-time and overall memory footprint.

We firstly compute the covariance function of the random field realisations based on an anisotropic exponential covariance using spatial averaging (Fig. 3a, d, g, j, m, 'Simulated') and compare it to the estimated covariance function using the analytical expression (5) for various number of harmonics (N_h) (Fig. 3a, d, g, j, m, 'Analytical'). The accuracy of the simulated spatial realisation depends on the number of harmonics in the summation (3). We sample spatial realisations of a 3-D isotropic random field on a regular grid with constant grid step (correlation length = [5, 5, 5] – as in Fig. 1b), to simplify the estimation of covariance function. In this case, the covariance can be computed over realisations just along one spatial direction. For correct spatial averaging the size of the domain must be significantly larger than the correlation lengths. Moreover, in order to achieve an accurate comparison to the analytical estimation several correlation lengths have

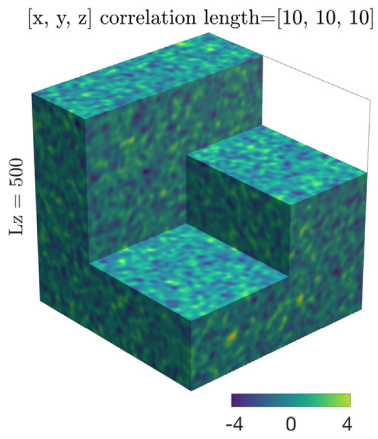

Fig. 2. Simulated random field using an isotropic Gaussian covariance function with correlation length of 10 in all 3 spatial dimensions within a cube of size [500, 500, 500] in x, y and z direction, respectively.

to be covered by the linear sizes of the computational and the estimated domains. We test 5 different number of harmonics (N_h) ranging from 10^2 (Fig. 3a–c) to 10^5 (Fig. 3m–o). We report for every N_h realisation the corresponding spatial distribution for both the xy (Fig. 3b, e, h, k, n) and the xz (Fig. 3c, f, i, l, o) slice. This experiment clearly shows the convergence of the method when a sufficiently large number of harmonics (N_h) is performed; the periodic noise pattern (aliasing) consequently vanishes from the spatial random distribution and the covariance estimations $C(r)$ plotted as function of the spatial radius r are in good agreement with the analytical results.

We secondly evaluate the sensitivity of the simulated random fields based on (a) an anisotropic exponential covariance function to the numerical grid resolution (Fig. 4). We consider 5 different realisations for numerical resolutions ranging from 32^3 (Fig. 4a–c) up to 1024^3 (Fig. 4m–o) grid points in 3-D. For each realisation we report the covariance function to be compared to the analytical estimation (Fig. 4a, d, g, j, m) as well as the spatial random field distribution for both the xy (Fig. 4b, e, h, k, n) and the xz (Fig. 4c, f, i, l, o) slices. We observe no significant influence of the numerical spatial resolution on the results affecting the 'Analytical' and 'Simulated' covariance functions. However, the spatial distribution of the random field is impacted by the low resolution realisations; variations below the grid resolution (dx) will not be detected. These tests indicate that our method allows to reproduce accurately the statistics of the random field even with a sparse grid resolution.

We in addition stress that the reported simulated random field covariance functions are not equal to 1 for $r = 0$ ($C(0) \neq 1$) in case a single and thus identical random number ($\lambda_1 = \lambda_2$) is used within the Box–Muller algorithm (19).

We repeat this second benchmark for the random field realisations based on (b) an isotropic Gaussian covariance (Fig. 5), and only show one realisation for a numerical resolution of 512^3 grid points in 3-D. We benchmark the covariance function to be compared to the analytical estimation (Fig. 5a) as well as the spatial random field distribution for both the xy (Fig. 5b) and the xz (Fig. 5c) slices. We report the accuracy of the random field generator based on spectral representations to simulate Gaussian covariance function and confirm the ability of the approach to handle various covariance functions.

We compare the performance of our random field generator relying on spectral representations with an effective and frequently used method based on the Fast Fourier Transform (see Section 3). To this

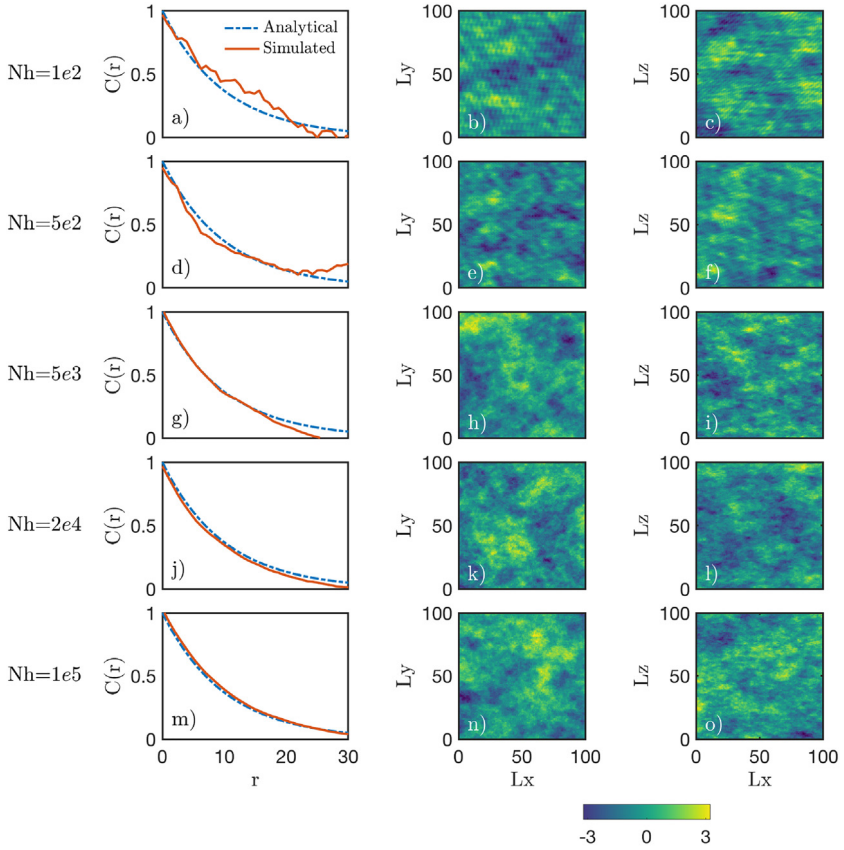

Fig. 3. Comparison of covariance functions $C(r)$ as function of spatial radius r for the simulated random fields versus the analytical expression. We compare the influence of the number of harmonics (N_h) on the random field realisations for the isotropic model configuration (Fig. 1b). We utilise a numerical grid resolution of 512^3 grid points in 3-D and constant grid steps.

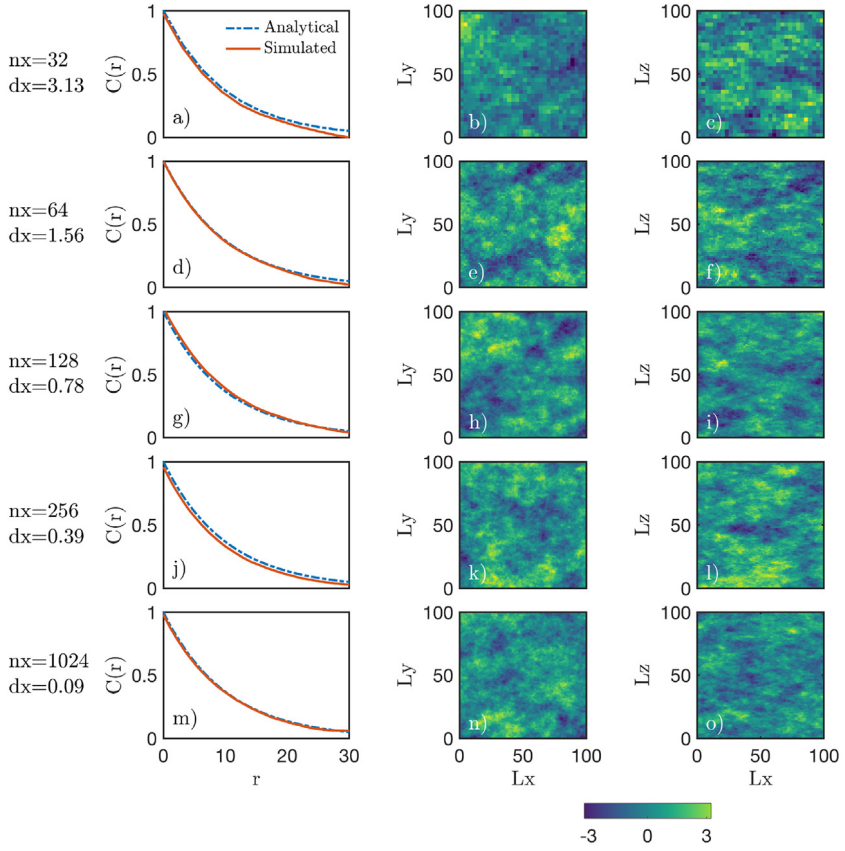

Fig. 4. Comparison of covariance functions $C(r)$ as function of spatial radius r for the simulated random fields versus the analytical expression. We compare the influence of refining the numerical grid resolution in 3-D on the simulated random field for the isotropic model configuration (Fig. 1b).

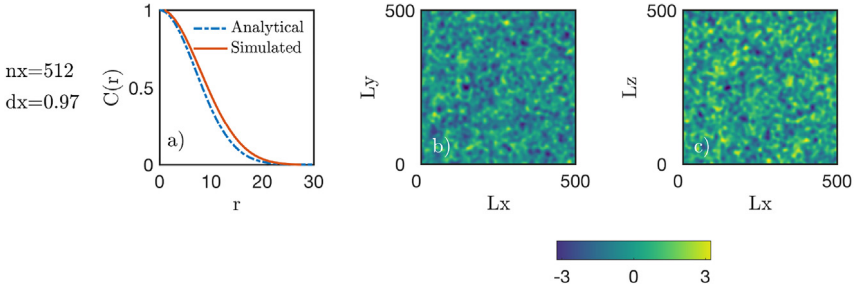

Fig. 5. Comparison of covariance functions $C(r)$ as function of spatial radius r for the simulated random fields versus the analytical expression. We compare the random field realisations for the model implementing the isotropic Gaussian covariance function (Fig. 2). We utilise a numerical grid resolution of 512^3 grid points in 3-D and constant grid steps.

end, we implemented a 3-D FFT-based random field generator using the CUDA FFT library cuFFT (Nvidia, 2018). Prior to evaluate the performance between the two approaches (spectral realisations and FFT), we benchmark the FFT-simulated exponential covariance function versus the analytical expression (Fig. 6). We show that our FFT-based implementation is in good agreement with the analytical expression in this example involving 512^3 grid points. Note that we had to increase the domain size to include 50 correlation lengths in order to converge towards accurate results.

We assess the performance of the random field simulator based on spectral representations (Section 2) comparing the memory footprint (Fig. 7) as well as the wall-time (Fig. 8) to the FFT-based simulator (Section 3). We report that both in single (SP) and double precision (DP) arithmetic the random field generator based on spectral representation (SRep) consistently utilises about seven times less memory compared to the FFT-based approach (Fig. 7). Also, both methods scale linearly with their respective memory footprints. The discrepancy in the memory footprint between the two methods mainly comes from the fact that only one 3-D field is mandatory for the spectral representation approach (20), while the FFT-based approach requires a more complex data layout involving complex numbers as well (21). We evaluated the memory footprint (in GB) for the spectral representation $\mathrm{m_{SRep}}$ and for the FFT-based $\mathrm{m_{FFT}}$ approaches, respectively, as following:

$$\mathrm{m_{SRep}} = \frac{n_x n_y n_z n_\mathrm{p}}{1024^3}\ , \tag{20}$$

$$\mathrm{m_{FFT}} = \frac{\left(5 n_x n_y n_z + 4 n_x n_y (n_z/2+1)\right) n_\mathrm{p}}{1024^3}\ , \tag{21}$$

where n_x, n_y, n_z is the grid resolution in the 3 spatial directions, x, y, z, respectively, and n_p is the arithmetic precision in bytes (single=4, double=8).

Benefits of lower memory utilisation are especially noticeable for large problem size as the memory footprint determines the maximal

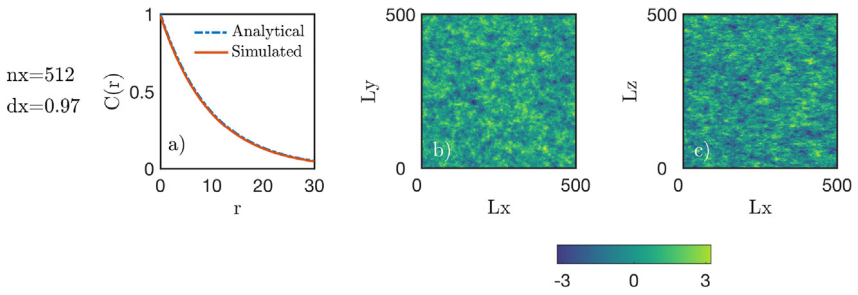

Fig. 6. Comparison of covariance functions $C(r)$ as function of spatial radius r for the FFT-based simulated random fields versus the analytical expression. We compare the random field realisations for the model implementing the anisotropic exponential covariance function. We utilise a numerical grid resolution of 512^3 grid points in 3-D and constant grid steps and a correlation length of [10,8,5] in x, y and z direction, respectively.

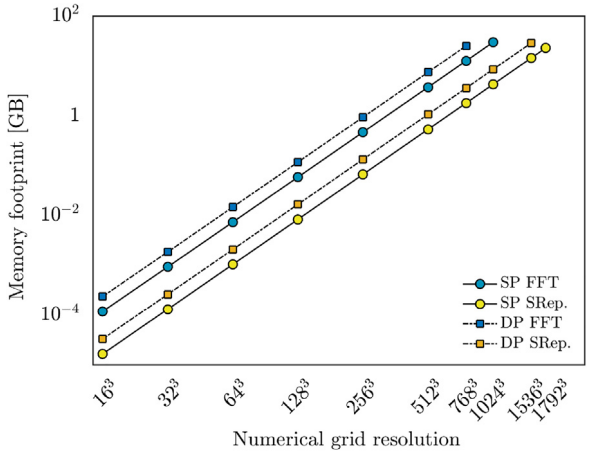

Fig. 7. Total memory footprint [GB] of the spectral representation (SRep) and FFT-based (FFT) 3-D random field GPU simulator. We report the global memory utilisation, varying the problem size from 16^3 to 1792^3 for both single precision (SP) and double precision (DP) arithmetic The spectral representation approach utilises only one 3-D field (20), while the FFT-based approach utilises the equivalent of 5 3-D fields (21).

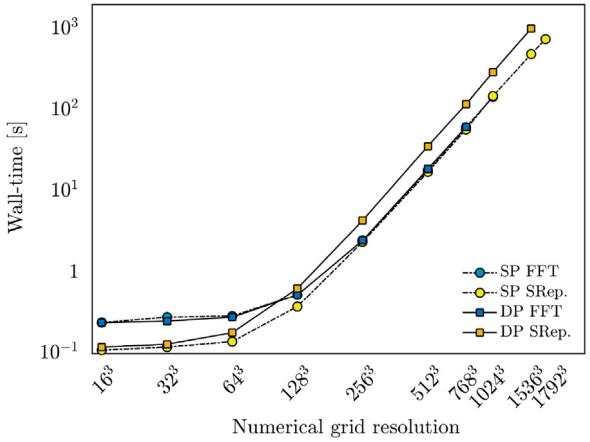

Fig. 8. Wall-time [s] of the spectral representation (SRep) and FFT-based (FFT) 3-D random field simulator on a Nvidia Tesla Volta V100 GPU. We report the time to solution, varying the problem size from 16^3 to 1792^3 for both single precision (SP) and double precision (DP) arithmetic.

problem size possible to resolve on a single GPU. The approach relying on spectral representation permits to resolve a 3-D problem of 1792^3 versus only 1024^3 for the FFT-based approach — close to a factor 2 (Fig. 7).

We then utilise the wall-time metric to report the time it takes in seconds to compute one realisation of the Gaussian random field using both approaches (Fig. 8). The timings are in good agreement between the two approaches, although the spectral representation in double precision is slightly off compared to the three other cases. A general trend shows the latency bound effects of all 4 tested configuration up to a problem size of about 128^3 in 3-D on the GPU. Then, we report a linear increase in time to solution for all methods and considered arithmetic precisions. We employed $N_h = 10'000$ for the spectral representation approach for this benchmark. Faster time to solution could be obtained by decreasing N_h, but this may lead to increased aliasing issues (see Section 5.2). Note that the scaling does not break even for the highest targeted resolution beyond the maximal domain size the FFT-based approach can handle.

We finally report the efficiency of the random field generator implementation on GPUs using the effective memory throughput as metric (Duretz et al., 2018). The effective memory throughput $\mathrm{MTP}_{\mathrm{eff}}$ evaluates the optimality of non-redundant data transfers from and to the GPU memory. The entire algorithm (Algorithm 1) is composed of 3 main blocks reported in Section 4. Lines 3–17 in Algorithm 1 generate 5 scalars (V_1, V_2, V_3, a, b) in a serial fashion on the CPU to be used in the parallel GPU kernel (Algorithm 3). The computationally more intense tasks (Algorithm 3) rely in each GPU thread accessing an entry of the Y_f array in parallel for each grid point of the domain. Local coordinates are used in computing the *tmp* scalar to update Y_f and write it back. This operation requires 2 memory accesses, one read, and one write per N_h harmonic. We can thus evaluate the minimal amount of memory n_{m} (in Bytes) needed to be transferred at each N_h harmonic $n_{\mathrm{m}} = 2n_x n_y n_z n_{\mathrm{p}}$. The effective memory throughput $\mathrm{MTP}_{\mathrm{eff}}$ (in GB/s) is then obtained as following:

$$\mathrm{MTP}_{\mathrm{eff}} = \frac{n_{\mathrm{m}} N_h}{n_{\mathrm{t}} 1024^3}\,, \tag{22}$$

where N_h is the number of iterations over the harmonics and n_{t} is the algorithm execution time in seconds. We compare $\mathrm{MTP}_{\mathrm{eff}}$ values obtained for the random field simulator for single (SP) and double (DP) precision executions (Fig. 9). We realise a strong scaling on a single Nvidia Tesla V100 (PCIe) GPU on which memory copy values are about 720 GB/s (dotted line in Fig. 9). We report that the $\mathrm{MTP}_{\mathrm{eff}}$ values saturated for both arithmetic precisions to 630 GB/s (88% of memory copy) for computational domains containing more than 400 grid points in all 3 dimensions.

6. Applications

We utilise the random field simulator to investigate the effect of acoustic wave scattering as function of the anisotropy and statistical properties of the random medium. We combine the random field simulator with a 3-D finite-difference acoustic wave propagation simulator in the time domain (FDTD). We rely on a second order in time and fourth order in space discretisation of the non-split pressure formulation (DeSanto, 1992). We include absorbing boundaries to avoid

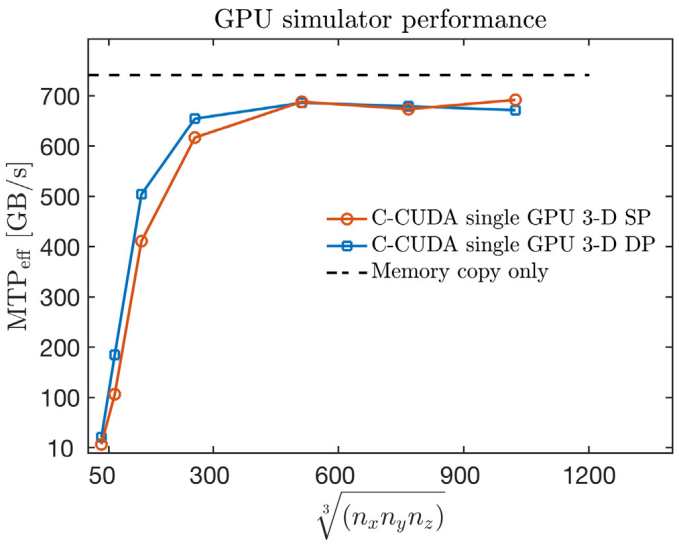

Fig. 9. Effective memory throughput MTP_{eff} [GB/s] of the implemented 3-D random field simulator on a Nvidia Tesla Volta V100 GPU. We report a strong scaling, varying the problem size from 32^3 to 1024^3 for both single precision (SP) and double precision (DP) arithmetic.

reflections of the wave at the artificial boundaries of the computational domain (Moczo et al., 2014). We use a cubic domain of $L_x = L_y = L_z = 3000$ m, discretised on 512^3 grid points in 3-D. The width of the absorbing boundaries is of 400 m. The time dependent source of a vertically ascending planar wave is located on the z-plane of coordinate $z = 0$, at the bottom of the domain for the first configuration (Fig. 10a) and at the top of the domain for the second configuration (Fig. 10b). We simulate a forward planar wave propagation for 3 types of random media displaying various correlation lengths and respecting identical box-size to correlation lengths ratios as the random fields depicted in Fig. 1.

We use a plane wave at the source plane to initiate the wavefield. The initial waveform $s(t)$ corresponds to a Gaussian wavelet with the peak frequency (f_0) of 10 Hz:

$$s(t) = s_0 e^{-8 f_0^2 (t-t_0)^2}, \tag{23}$$

where s_0 is the initial amplitude and t_0 is the wave onset time.

We perform two forward simulations for each of the 3 utilised random fields; the first simulation is performed in homogeneous background velocity model (3200 ms^{-1}) while the second simulation includes the random velocity heterogeneities. This approach allows us to resolve the scattered wavefield (coda wave) by subtracting the background wavefield (direct wave) from the signal obtained in the randomly perturbed medium. We qualitatively report the contours of the pressure envelope (positive and negative iso-surfaces) for the coda wave evolving with time (vertical axis) through a vertically correlated (Fig. 11a), isotropic (Fig. 11b) and horizontally layered (Fig. 11c) random medium.

In addition, we record the coda wave energy envelopes using a root mean square (RMS) ensemble average for 20 realisations for both investigated configuration; both at half the domain height ($z = 1100$ m) along the x-axis (Fig. 12a, c, e) and at source ($z = 0$ m) location (Fig. 12b, d, f) for the 3 distinct correlation length configurations (Fig. 11a, b, c). We report a clear trend that energy envelopes are larger for the random medium displaying a minimal correlation length in the direction of the propagating wave compared to configurations where the correlation length is maximal along direction of the propagating wave, here the z-axis.

7. Discussion

We have considered geometrical anisotropy with an idea that the heterogeneity in the Earth can be represented in terms of continuous stochastic random heterogeneities. The analysis of seismic coda was particular fruitful to infer quantitative measures of the seismic scattering attenuation in the heterogeneous Earth (Fehler and Sato, 2003). Scattering of seismic waves in the crust assuming random heterogeneity has previously been extensively studied (e.g. Frankel and Clayton, 1986). Meschede and Romanowicz (2015) use spectral Fourier method combined with the Karhunen–Loève expansion to construct non-stationary models on 3-D grids for global seismology applications. However, the size of covariance matrix and thus spatial resolution was limited by the computer RAM in their simulations (Meschede and Romanowicz, 2015). Our method is free of this limitation and allows for an unstructured mesh and a variable resolution across the model domain.

The interaction of seismic wave encountering a heterogeneity of comparable or several times smaller size than the seismic wave length produces secondary scattered waves. The scattered wave train recorded after the first arrival of direct wave forms coda. Numerical simulations of coda are useful to examine the effects of small-scale structures on seismic waveforms. The scattering energy distribution and coda level in random media with different correlation lengths in radial and tangential direction depends on the incidence angle of the direct wave (Hong and Wu, 2005). Thus, the coda energy variation in time can be explained by the energy partitioning between forward and backward scattered waves. The aspect ratio between the radial and tangential scales controls the strength of the backscattering. Scattered waves propagating backward or forward can be observed in receivers placed behind or in front of the scatterer. The forward scattered waves with small scattering angle arrive just after the direct wave. The numerical

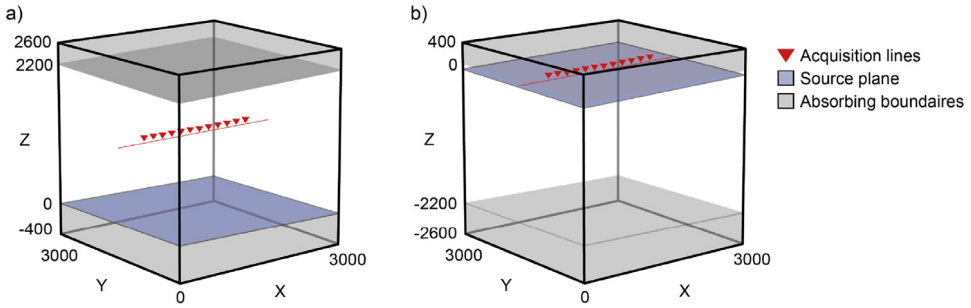

Fig. 10. Initial conditions for the 3-D wave propagation model configuration including acquisition lines, source plane and absorbing boundaries. (a) Plane wave coming from the bottom and acquisition line at mid-domain depth mimics a teleseismic wave observation in seismology. (b) Acquisition line and source plane located on identical depths mimics a relevant configuration for multi-channel seismic reflection. Note that for better readability, the absorbing boundaries are only depicted in the vertical z direction but are implemented in a similar fashion in the x and y directions.

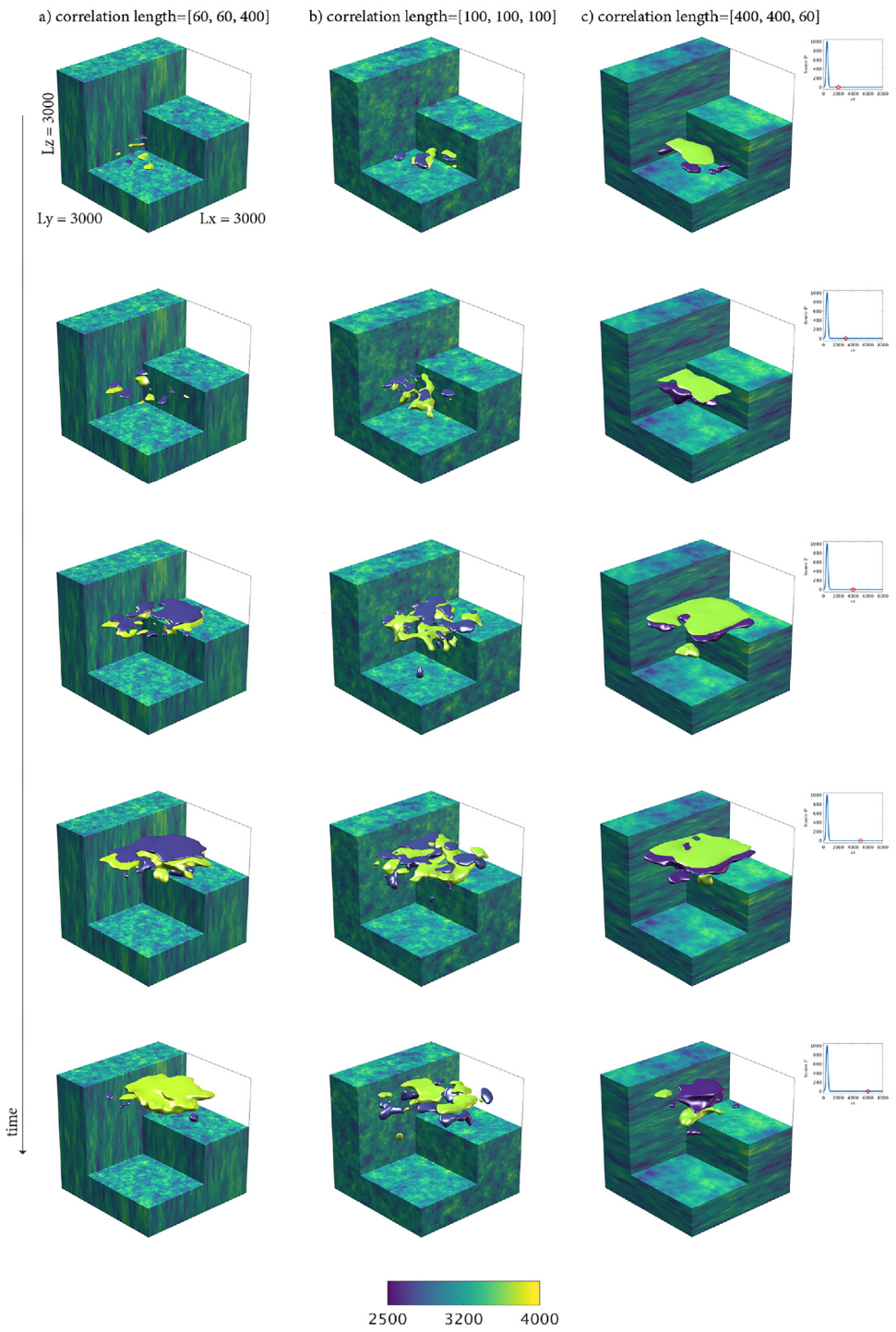

Fig. 11. FDTD wave propagation in 3 distinct realisations of random media corresponding to the identical (a, b, c) ratios compared to the vertical box-size as depicted in Fig. 1. The random fields are assigned to the seismic velocity within the forward simulations within the range of 2500–4000 m s^{-1}. The planar wave source located at $z = 0$ m (configuration as in Fig. 10a) produces a scattered wavefield contoured for one positive and one negative pressure isosurface that evolves through time (vertical axis). The rightmost column displays the time dependent amplitude of the source perturbation. Animations related to this figure are available as supplementary material.

simulation of acoustic scattering is also important for better understanding the relative strengths of extrinsic (scattering) and intrinsic (absorption) seismic attenuation.

The first configuration (Fig. 10a) including a plane wave coming from the bottom of the model mimics a teleseismic wave observation in earthquake seismology. The decay of seismic scattered coda waves represented by the energy envelops provides information on statistical properties of the Earth's mantle heterogeneity (Hong and Wu, 2005). In particular, backward scattering is stronger for planar heterogeneities (layered structures) whereas the vertically oriented structures (plumes, slabs) produce mainly forward scattering (Hong and Wu, 2005; Meschede and Romanowicz, 2015). Seismological studies suggest that the upper mantle contains strong heterogeneity of elastic properties at length scales from a few kilometres to tens of thousands kilometres (Mancinelli et al., 2016). The origin of small-scale heterogeneities in the mantle was attributed to both solid-state thermal convection facilitated by thermally activated creep processes and chemical anomalies forming as a result of partial melting of the mantle

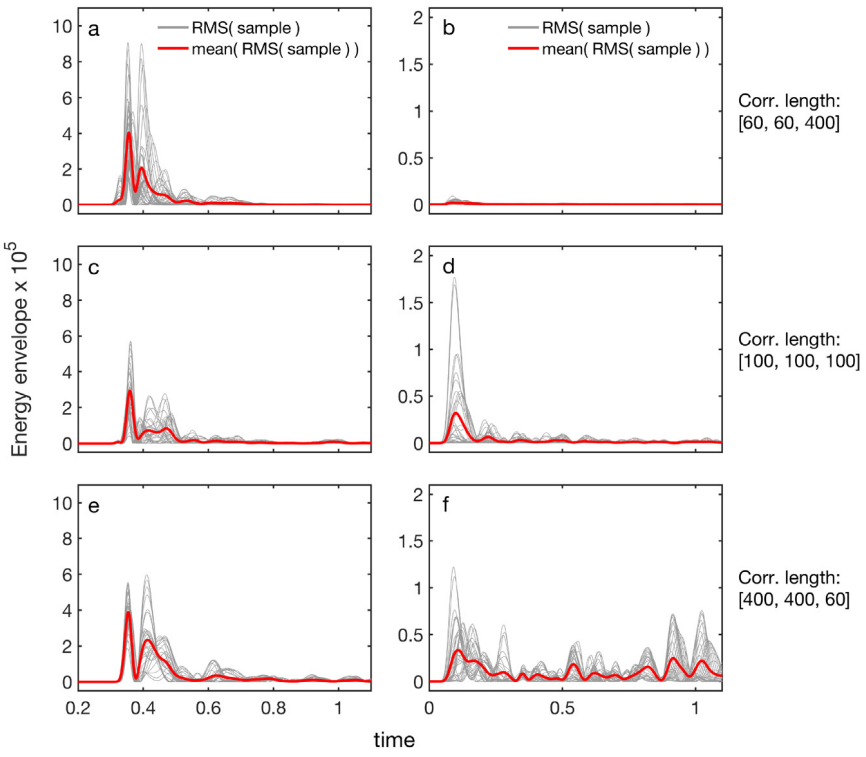

Fig. 12. Coda wave energy envelopes for resulting from the planar acoustic wave propagation for random media with correlation lengths in $[x, y, z]$ directions of (a–b) [60, 60, 400] m, (c–d) [100, 100, 100] m and (e–f) [400, 400, 60] m. The selected recording locations are at half the domain height (a, c, e) and at the source plane (b, d, f). The samples include RMS values of the full set of recorded waves for 20 realisations. The red line displays the RMS ensemble average. When applied to the studies of the Earth's mantle heterogeneities and P coda seismological observations, the model parameters upscale to be 300 km for the model vertical and lateral sizes, and the correlation lengths in $[x, y, z]$ directions become (a) [6, 6, 40] km, (c) [10, 10, 10] km and (e) [40, 40, 6] km.

rocks (Khan and Deschamps, 2015). Numerical simulations Schmalzl and Hansen (1994) emphasised a scale-dependent efficiency of chemical mixing by thermal convection in the Earth's mantle. The sensitivity of teleseismic P-wave coda to the statistical properties (e.g. correlation function) of the mantle heterogeneity (Hedlin et al., 1997; Ricard et al., 2014; Mancinelli et al., 2016) can offer useful constraints on the efficiency of mantle mixing across a broad range of scales and, thus, elucidate geochemical evolution of the Earth.

The second configuration (Fig. 10b) is relevant for active seismic monitoring of hydrocarbon reservoirs. Primary migration of hydrocarbons formed in the source rock occurs into a reservoir where oil and gas are accumulated if an overlying low-permeability seal (cap rock) exists. However, hydrocarbons may sometimes escape from the reservoirs through the cap rocks up to the surface by various mechanisms such as fracture, diffusion and porosity waves (Räss et al., 2018). An active leakage process is potentially hazardous and must be considered in any prospect risk assessment. A hydrocarbon leakage can sometimes be directly observed as pockmarks and seepage plumes in the water column. Otherwise, 3-D time-lapse seismic reflection data can be used for remote monitoring of the leakage processes that occur in the subsurface (Løseth et al., 2009). The standard processing of the seismic data includes the summation of coherent signal corresponding to the waves reflected and back-scattered in the sedimentary layer including both the stratified and 3-D fine-scale heterogeneities.

Zones of dimmed seismic amplitudes where the reflections from stratigraphic layers are significantly weaker than in adjacent areas are often encountered in seismic sections above leaking hydrocarbon reservoirs (Løseth et al., 2009). The amplitude dimming was attributed to a localised fluid or gas flow in the sediments based on a wealth of empirical data but the physical mechanisms behind are not well understood (Løseth et al., 2009). The relation between physical properties inside the zones of fluid flow and their expression in stacked multichannel reflection data is complex and non-unique. A realistic numerical experiment requires a 3-D geometry since the seismic energy scattered on small-scale pipe and vertical sheet seismic anomalies is different.

In Fig. 12 the amplitudes of recorded back-scattered are significantly attenuated in the case of vertically oriented structures compare to the isotropic and planar horizontal heterogeneities despite that the mean bulk acoustic velocity remains the same. This has an important implication for understanding the effective elastic properties of the sedimentary systems affected by localised pore pressure changes and active fluid flow based on 3-D time-lapse seismic data.

8. Conclusion

Realistic numerical modelling of the Earth's spatial heterogeneity requires a length scale resolution across more than 4 orders of magnitude. In 3-D geometries, the computation is only feasible using parallel implementation of numerical algorithms. We suggest an efficient numerical method based on a randomisation technique (Sabelfeld, 1991) which allows to simulate the Earth's heterogeneity down to an arbitrary small scale assuming that the medium can be described as a random Gaussian field with a known correlation function or power spectrum. The GPU-accelerated numerical algorithm is described to simulate spatial realisations of a 3-D anisotropic homogeneous Gaussian random field in Cartesian coordinates. We showcase the ability of the approach to handle both exponential and Gaussian covariance functions. We confirm good performance results of the proposed method compared to a FFT-based approach, showing about one order of magnitude lower memory usage and comparable wall-times. Moreover, the proposed method to generate Gaussian random fields based on spectral representation will scale linearly on distributed memory machines, as no communication is involved to reach the solution, which may not be the case for FFT-based approaches. The presented geophysical examples support the efficiency of the method and report the sensitivity of the

recorded scattered seismic wavefields on the orientation and aspect ratio of the anisometric stochastic heterogeneity. These results can be applied to interpret seismic data across a wide range of scales: from a hydrocarbon reservoir to the upper mantle.

Computer code availability

The presented GRFS (exponential and Gaussian covariance) algorithm and computer codes (serial Matlab & parallel GPU-based CUDA C) are provided as supplementary material and available for download from Bitbucket at https://bitbucket.org/lraess/grfs and from the Swiss Geocomputing Centre website http://wp.unil.ch/geocomputing/software/grfs/. Both the exponential and Gaussian covariance implementations are shared. The GPU cuFFT-based benchmarking algorithm as well as the GPU-based 3-D acoustic wave propagation software can be obtained upon request from the authors.

CRediT authorship contribution statement

Ludovic Räss: Conceptualization, Investigation, Methodology, Project administration, Software, Validation, Visualization, Writing - original draft, Writing - review and editing. **Dmitriy Kolyukhin:** Methodology, Software, Validation, Writing - original draft, Writing - review and editing. **Alexander Minakov:** Conceptualization, Investigation, Methodology, Project administration, Supervision, Validation, Writing - original draft, Writing - review and editing.

Acknowledgements

The authors thank Thomas Bodin as well as two anonymous reviewers for their valuable feedback that permitted to enhance the first version of this manuscript. LR acknowledges support from the Swiss National Science Foundation's Early Postdoc.Mobility Fellowship 178075 and computational resources from the Swiss Geocomputing Centre. DK acknowledges support from RFBR, Russia (grants no. 15-55-20004, 18-05-00031) and IPGG project AAAA-A16-116122810045-9. AM acknowledges support by the Research Council of Norway through its Centers of Excellence funding scheme, project 223272.

Appendix A. Supplementary data

Supplementary material related to this article can be found online at https://doi.org/10.1016/j.cageo.2019.06.007.

References

Box, G.E.P., Muller, Mervin E., 1958. A note on the generation of random normal deviates. Ann. Math. Statist. 29 (2), 610–611.
de Carvalho Paludo, L., Bouvier, V., Cottereau, R., Clouteau, D., 2015. Efficient parallel generation of random field of mechanical properties for geophysical application. 12e Colloque national en calcul des structures, CSMA, Giens, France.
Christakos, G., 2012. Random Field Models in Earth Sciences. Courier Corporation.
De Siena, L., Del Pezzo, E., Thomas, C., Curtis, A., Margerin, L., 2013. Seismic energy envelopes in volcanic media: in need of boundary conditions. Geophys. J. Int. 195 (2), 1102–1119.
DeSanto, J.A., 1992. Scalar Wave Theory. Springer.
Deutsch, C.V., Cockerham, P.W., 1994. Practical considerations in the application of simulated annealing to stochastic simulation. Math. Geol. 26 (1), 67–82.
Dowd, P., Pardo-Igúzquiza, E., Xu, C., 2003. Plurigau: a computer program for simulating spatial facies using the truncated plurigaussian method. Comput. Geosci. 29 (2), 123–141.
Dowd, P.A., Xu, C., Mardia, K.V., Fowell, R.J., 2007. A comparison of methods for the stochastic simulation of rock fractures. Math. Geol. 39 (7), 697–714.
Duretz, T., Räss, L., Podladchikov, Y.Y., Schmalholz, S.M., 2018. Resolving thermo-mechanical coupling in two and three dimensions: Spontaneous strain localisation owing to shear heating. Geophys. J. Int..
Eyink, G., Goldenfeld, N., 1994. Analogies between scaling in turbulence, field theory, and critical phenomena. Phys. Rev. E 50 (6), 4679.
Fehler, M., Sato, H., 2003. Coda. Pure Appl. Geophy. 160 (3–4), 541–554.
Frankel, A., Clayton, R.W., 1986. Finite difference simulations of seismic scattering: Implications for the propagation of short-period seismic waves in the crust and models of crustal heterogeneity. J. Geophy. Res. Solid Earth 91 (B6), 6465–6489.
Hansen, T.M., Mosegaard, K., Cordua, K.S., 2008. Using geostatistics to describe complex a priori information for inverse problems. In: VIII International Geostatistics Congress, Vol. 1. Mining Engineering Department, University of Chile, pp. 329–338.
Hedlin, M.A., Shearer, P.M., Earle, P.S., 1997. Seismic evidence for small-scale heterogeneity throughout the Earth's mantle. Nature 387 (6629), 145.
Holliger, K., Levander, A.R., Goff, J.A., 1993. Stochastic modeling of the reflective lower crust: petrophysical and geological evidence from the Ivera Zone (northern Italy). J. Geophys. Res. Solid Earth 98 (B7), 11967–11980.
Hong, T.K., Wu, R.S., 2005. Scattering of elastic waves in geometrically anisotropic random media and its implication to sounding of heterogeneity in the Earth's deep interior. Geophys. J. Int. 163 (1), 324–338.
Katz, R.F., Weatherley, S.M., 2012. Consequences of mantle heterogeneity for melt extraction at mid-ocean ridges. Earth Planet. Sci. Lett. 335, 226–237.
Khan, A., Deschamps, F., 2015. The Earth'S Heterogeneous Mantle: A Geophysical, Geodynamical, and Geochemical Perspective. Springer.
Kolyukhin, D., Sabelfeld, K., 2005. Stochastic flow simulation in 3D porous media. Monte Carlo Methods Appl. 11 (1), 15–37.
Kraichnan, R.H., 1970. Convergents to turbulence functions. J. Fluid Mech. 41 (1), 189–217.
Kramer, P.R., Kurbanmuradov, O., Sabelfeld, K., 2007. Comparative analysis of multiscale Gaussian random field simulation algorithms. J. Comput. Phys. 226 (1), 897–924.
Kurbanmuradov, O., Sabelfeld, K., Koluhin, D., 1997. Stochastic Lagrangian models for two-particle motion in turbulent flows. Numerical results. Monte Carlo Methods Appl. 3 (3), 199–224.
Le Ravalec, M., Noetinger, B., Hu, L.Y., 2000. The FFT moving average (FFT-MA) generator: An efficient numerical method for generating and conditioning Gaussian simulations. Math. Geol. 32 (6), 701–723.
Løseth, H., Gading, M., Wensaas, L., 2009. Hydrocarbon leakage interpreted on seismic data. Mar. Pet. Geol. 26 (7), 1304–1319.
Mancinelli, N., Shearer, P., Liu, Q., 2016. Constraints on the heterogeneity spectrum of Earth's upper mantle. J. Geophy. Res. Solid Earth 121 (5), 3703–3721.
Mantoglou, A., Wilson, J.L., 1982. The turning bands method for simulation of random fields using line generation by a spectral method. Water Resour. Res. 18 (5), 1379–1394.
Marcotte, D., Allard, D., 2018. Gibbs sampling on large lattice with GMRF. Comput. Geosci. 111 (June 2017), 190–199. http://dx.doi.org/10.1016/j.cageo.2017.11.012.
Meschede, M., Romanowicz, B., 2015. Non-stationary spherical random media and their effect on long-period mantle waves. Geophys. Suppl. Mon. Not. R. Astron. Soc. 203 (3), 1605–1625.
Minakov, A., Keers, H., Kolyukhin, D., Tengesdal, H.C., 2017. Acoustic waveform inversion for ocean turbulence. J. Phys. Oceanogr. 47 (6), 1473–1491.
Minakov, A., Yarushina, V., Faleide, J.I., Krupnova, N., Sakoulina, T., Dergunov, N., et al., 2018. Dyke emplacement and crustal structure within a continental large igneous province, northern Barents Sea. Geol. Soc. London Spec. Publ. 460 (1), 371–395.
Moczo, P., Kristek, J., Galis, M., 2014. The Finite-Difference Modelling of Earthquake Motions: Waves and Ruptures. Cambridge.
Monin, A., Yaglom, A., 1971. Statistical Fluid Mechanics of Turbulence, Vol. 2.
Nvidia, 2018. CUDA Programming Guide.
Phoon, K., Huang, S., Quek, S., 2002. Simulation of second-order processes using Karhunen–Loeve expansion. Comput. struct. 80 (12), 1049–1060.
Phoon, K., Huang, H., Quek, S., 2005. Simulation of strongly non-Gaussian processes using Karhunen–Loeve expansion. Probab. Eng. Mech. 20 (2), 188–198.
Räss, L., Simon, N.S., Podladchikov, Y.Y., 2018. Spontaneous formation of fluid escape pipes from subsurface reservoirs. Sci. Rep. 8 (1), 11116.
Ricard, Y., Dur, S., Montagner, J.P., Chambat, F., 2014. Is there seismic attenuation in the mantle? Earth Planet. Sci. Lett. 388, 257–264.
Robin, M., Gutjahr, A., Sudicky, E., Wilson, J., 1993. Cross-correlated random field generation with the direct fourier transform method. Water Resour. Res. 29 (7), 2385–2397.
Rubinstein, R.Y., 1981. Simulation and the Monte Carlo Method, first ed. John Wiley & Sons, Inc., New York, NY, USA, ISBN: 0471089176.
Sabelfeld, K.K., 1991. Monte Carlo Methods in Boundary Value Problems. Springer.
Sabelfeld, K., Loshchina, N., 2010. Stochastic iterative projection methods for large linear systems. Monte Carlo Methods Appl. 16 (3–4), 343–359.
Sato, H., Fehler, M.C., Maeda, T., 2012. Seismic Wave Propagation and Scattering in the Heterogeneous Earth, Vol. 496. Springer.
Sava, P., Poliannikov, O., 2008. Interferometric imaging condition for wave-equation migration. Geophysics 73 (2), S47–S61.
Schmalzl, J., Hansen, U., 1994. Mixing the Earth's mantle by thermal convection: A scale dependent phenomenon. Geophys. Res. Lett. 21 (11), 987–990.
Simonovski, I., Cizelj, L., 2005. Correlation length estimation in a polycrystalline material model. In: Proc. of the Int. Conf. Nuclear Energy for New Europe, Bled, Slovenia.
Strebelle, S., 2002. Conditional simulation of complex geological structures using multiple-point statistics. Math. Geol. 34 (1), 1–21.

Tang, Y., Atkinson, P.M., Wardrop, N.A., Zhang, J., 2013. Multiple-point geostatistical simulation for post-processing a remotely sensed land cover classification. Spat. Statist. 5, 69–84.

Tran, N., Chen, Z., Rahman, S., 2007. Practical application of hybrid modelling to naturally fractured reservoirs. Pet. Sci. Technol. 25 (10), 1263–1277.

Tyaginov, S., Vexler, M., Sokolov, N., Suturin, S., Banshchikov, A., Grasser, T., et al., 2009. Determination of correlation length for thickness fluctuations in thin oxide and fluoride films. J. Phys. D: Appl. Phys. 42 (11), 115307.

Xiu, D., Karniadakis, G.E., 2002. Modeling uncertainty in steady state diffusion problems via generalized polynomial chaos. Comput. Methods Appl. Mech. Engrg. 191 (43), 4927–4948.